# Reconstruction of Wind Tunnel Tests using CFD for a Reusable First Stage during Rocket Retro- Propulsion

*Tamas Bykerk*[⋆†]*, Daniel Kirchheck*[^] *and Sebastian Karl*[⋆]
[⋆]*Deutsches Zentrum für Luft und Raumfahrt (DLR)*
*Institute of Aerodynamics and Flow Technology, Göttingen, Germany*
[^]*Deutsches Zentrum für Luft und Raumfahrt (DLR)*
*Supersonic and Hypersonic Technologies Department, Cologne, Germany*
tamas.bykerk@dlr.de · daniel.kirchheck@dlr.de · sebastian.karl@dlr.de
[†]Corresponding author

## Abstract

The RETPRO project (Validation of Wind Tunnel Test and CFD Techniques for Retropropulsion), as part of ESA's Future Launcher Preparatory Programme, aims at preparing the tools, necessary for a reliable design and simulation of future rocket launchers or spacecraft. A particular focus is assigned to vertical take-off and landing configurations using retro propulsion as part of their control concept for entry, descent, and landing manoeuvres. Wind tunnel tests and computational fluid dynamics are used to generate a comprehensive aerodynamic database, which is required for flight dynamics simulations, enabling mission and performance analyses of possible future launcher designs. This paper focuses on the presentation and discussion of steady-state numerical simulation results which reconstruct selected wind tunnel tests during both powered and unpowered descent phases. The CFD simulations cover a Mach number range from 2 up to 7, with dry air used to model the exhaust plume. Typical flow topologies and features are discussed, with quantitative results coming from a comparison of force balance and surface pressure measurements between experimental results and CFD simulations. Schlieren images from the experiments are used to evaluate the plume structure and shock stand-off distances. For the unpowered descent cases the agreement between schlieren images, force and pressure measurements is extremely strong. During powered descent the basic plume structure is captured well despite the highly unsteady and fluctuating flow field. Pressure and force measurements gave mixed results, but overall the studies show that RANS simulations perform well compared to experimental data.

## 1. Introduction

The recent success of several commercial launchers in landing, recovering and relaunching complete main stages has renewed the interest in the study of re-usable space transportation concepts. As shown by several systems, a restriction to the recovery of the first stage and the application of retro-propulsion for landing appears to be a promising concept for low-cost, robust and flexible vehicles. Commercial launch vehicles, such as the SpaceX Falcon 9, has inspired the development of the vertical take-off and landing (VTVL) re-usable launch vehicle (RLV). The recovery of the first stage is achieved through strategic retro-propulsion burns, control surface deflections and deployable landing legs to accomplish a precision landing. The nature of this trajectory introduces complex flow topologies through a large range of Mach numbers, requiring a strong understanding of the vehicle aerodynamics, plume behaviour and vehicle stability.[1]

The recovery of the first stage booster is a complex task which relies heavily on the successful implementation of a control system. This requires engineers to have intimate knowledge of vehicle aerodynamics, the effect of control surface deflections and the use of propulsion systems for vehicle deceleration and attitude control. This data is typically consolidated in an aerodynamic database, where derivatives are compiled according to Mach number, Angle of Attack (AoA), thrust setting and control surface inclination angle. Due to the complexity and cost of gathering this data from full scale flight tests, results from high-fidelity CFD predictions play a large role in the vehicle design. These datasets are complemented by ground test results which further serve as a basis for CFD accuracy assessment and validation. A close interaction of wind tunnel based and CFD investigations enables the reduction of prediction uncertainties and extrapolation of ground test data to flight scales.

While there is substantial experience in load predictions for hypersonic capsule or winged type re-entry concepts, retro-propulsion maneuvers are a particularly challenging problem for both CFD and ground based testing. This is primarily due to the complex fluid mechanical and thermo-chemical interaction between the exhaust plumes and the free stream. During retro-propulsion phases, large parts of the vehicle are immersed in its exhaust gases. Large recirculation regions and zones of flow reversal significantly affect the heat load distribution and aerodynamic characteristics. Furthermore, the divergence of the exhaust jets at low ambient pressures gives rise to strong plume-plume interactions in the vicinity of the launcher base.

In this context, the RETPRO project aims at the further development and validation of experimental and numerical simulation techniques which are needed for the aerodynamic and aerothermal design of re-usable launch systems with retro-propulsion.[2] RETPRO is carried out under a programme of and funded by the European Space Agency - through the Future Launchers Preparatory Programme. RETPRO is one of a few studies within Europe looking at better understanding the requirements for the design of VTVL RLVs.[3,4]

This paper focuses on the presentation and discussion of steady-state numerical simulation results which reconstruct selected wind tunnel tests during both powered and unpowered descent phases through a Mach number range of 2 to 7. First an overview of the RETPRO vehicle is presented. This is followed by an introduction to the CFD methodologies employed to recreate selected wind tunnel tests (WTT). Finally the results are discussed and conclusions are drawn on the correlations seen between experimental and numerical datasets.

## 2. RETPRO Vehicle

The RETPRO vehicle is of a two stage design with a re-usable first stage. Four grid fins are used for attitude control and braking, while four retractable legs are intended for the vertical landing. The shape is presented in Figure 1.

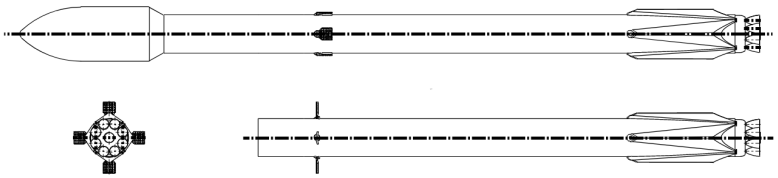

Figure 1: Overview of the RETPRO vehicle

An overview of the full sized vehicle geometric properties is summarised below in Table 1. The wind tunnel model has been scaled by a factor of 80.

Table 1: This is a table example

| **Property** | **Stage 1** | **Stage 2** |
|---|---|---|
| Height (m) | 47 | 23 |
| Diameter (m) | 3.66 | 3.66/5.20 |
| Number of Engines | 9 | 1 |

## 3. Methodology

### 3.1 Numerical Model

The TAU code is a second order finite-volume solver for the Euler and Navier-Stokes equations which includes a comprehensive range of RANS-based or scale resolving turbulence models. It uses unstructured computational grids to facilitate the analysis of complex geometries and is highly optimized for the application on massively parallel HPC systems. TAU has been successfully applied to a wide range of sub-to-hypersonic flow problems, both in scientific and industrial applications, including the analysis of re-usable launcher configurations.

The baseline set of numerical models which have been applied for the present investigations provides accurate and robust treatment for all flow conditions as defined in the CFD test matrix with free stream Mach numbers ranging from 2 to 7. The calculation of the inviscid fluxes in the finite volume framework is based on the application of the

AUSMDV flux vector splitting scheme together with MUSCL gradient reconstruction to achieve second order spatial accuracy. Viscous fluxes are treated with a low-dissipation central discretization scheme.

Turbulence was modelled with a Spalart-Allmaras one-equation RANS model in low Reynolds formulation. This model provides a good compromise between numerical efficiency and accuracy and is particularly applicable to flows with strong compression shocks. The model completely resolves the structure of the turbulent boundary layer including the laminar sub-layer. Thus, an adequate setup of the numerical grid is required which is achieved by using prismatic sub-layers close to the wall with a first dimensionless wall spacing of y+ in the order of one and a wall normal stretching ratio of grid cells of less than 1.3. The wall temperature was set to 300K and heat flux was assumed to be isothermal. The wall temperature was chosen based on the expected ambient air conditions and the assumption that the wall temperature would not vary significantly during the tests. Given that the test cases here are based on a 0 degree AoA condition (the first angle tested in the AoA sweeps) and the short test times, the wall temperature and heat flux assumption is valid.

The freestream air is treated as a perfect gas with a ratio of specifics heats equal to 1.4. Nozzle exhaust, where applicable, has been modelled by imposing the exit flow conditions of the thrust nozzles at their respective exit planes in the computational domain of the launcher. The radial distribution of the axial and radial velocity, exit pressure and temperature was determined by separate analyses of the flow inside the thrust nozzle, which provides an accurate representation of the exhaust jets in the three dimensional computations. The operating conditions at the nozzle reservoir were taken directly from the experimental datasets.

### 3.2 Axis System and reference values

Numerical results presented in this paper have been calculated using the axis convention used for the wind tunnel tests in accordance with Figure 2. Here the origin is located at the top most part of the first stage at the first and second stage junction. The axial force is the measurement of interest for the cases presented here.

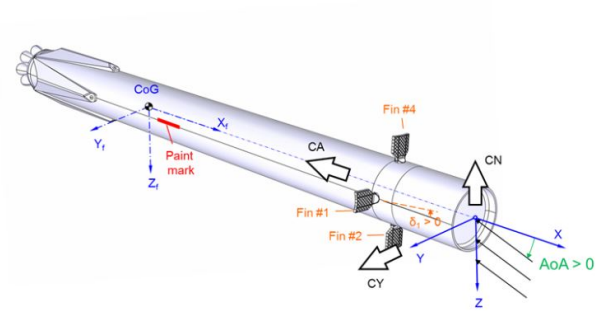


Figure 2: Axis convention used for wind tunnel tests

The reference values for the wind tunnel model are summarised in Table 2. A short model was used for the H2K tests, while a longer model was built for the TMK campaign. As a result, two centre of gravity (CoG) locations are presented, with the CoG measured from the origin as shown in Figure 2.

Table 2: Reference values for coefficient calculations

| Variable | Value | Units |
|---|---|---|
| Reference Area | $1.644 \times 10^{-3}$ | $m^2$ |
| Reference Length | $4.575 \times 10^{-2}$ | m |
| CoG (H2K) | -0.2032 | m |
| CoG (TMK) | -0.3760 | m |

### 3.3 Internal Flow

The numerical studies which reconstruct the H2K tests required the outflow conditions at the nozzle exits to model the plume structure. The cases presented here all had three active nozzles which were fed pressurised air through a main internal flowpath before being divided and ejected. To simplify the workflow and reduce computational expense, a 2D axis-symmetric setup of a single nozzle was used and carried over to each of the active nozzles. The grid used for these investigations are provided below in Figure 3.

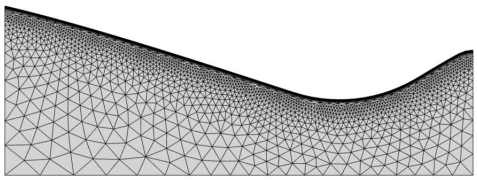

Figure 3: Single nozzle grid used for internal flowpath

### 3.4 3D External Flow

Based on unpublished precursor studies, two model variants were considered in these studies. The first is the short vehicle tested in H2K, with the second, longer model used in the TMK campaigns. The models used for the CFD simulations have been defeatured to aid the meshing process, with the sensor housings and the split at the baseplate removed. Finally, the fin connecting the sting to the tunnel infrastructure has been removed. This is permitted as it is far downstream of the model and the flow features which develop around it are not expected to impact the force or pressure measurements. Figure 4 presents the computer model used to generate the CFD grid with the model installed in the wind tunnel.


Figure 4: Comparison of computer model with wind tunnel setup

All test cases presented in this paper are with a symmetric vehicle configuration and no AoA. As a result, all computations were completed using a quarter grid.

## 4. Results and Discussion

This section provides a detailed overview of the CFD results obtained using the DLR Tau solver. A comparison between CFD and WTTs is provided for pressure and force measurements, as well as the density gradient field around the vehicle.

### 4.1 Baseline Mach 2

Figure 5 shows a side-by-side comparison of the CFD and WTT data for the Mach 2 case, where the shock stand off distances lie extremely close to one another. The presence of a detached bow shock at the gridfins is also clearly visible in both numerical and experimental studies. This will be discussed in further detail in the paragraphs which follow.

Figure 5: Schlieren photograph comparison for Mach 2 baseline case

Figures 6 and 7 present a direct comparison of the pressure coefficient data from WTTs and CFD. The correlation for the datapoints in the base and mid region is extremely strong, while the probes located around the grid fins show conflicting results.

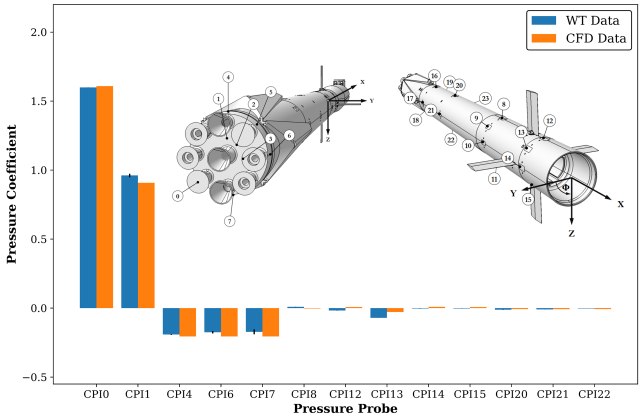


Figure 6: Surface pressure coefficient comparison for Mach 2 baseline case for large magnitude pressure coefficients

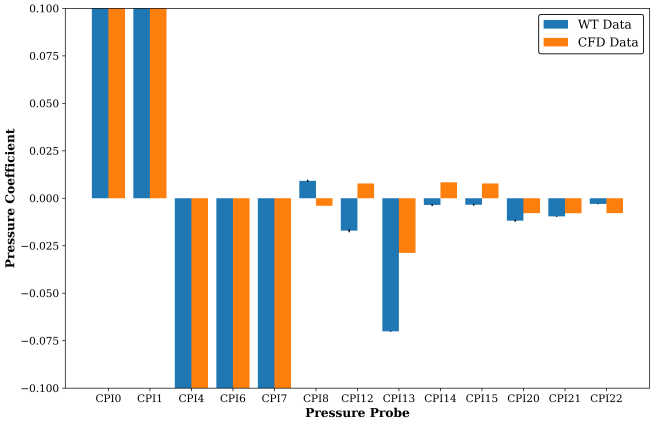


Figure 7: Surface pressure coefficient comparison for Mach 2 baseline case for small magnitude pressure coefficients

To further investigate the reason behind this, labelled surface contours of pressure coefficient are shown in Figure 8. The surface pressure in this region is dependent on the behaviour of the flow and shock structures in and around the gridfins. Variations in the flow topology are goverened by the upstream Mach number, with large changes expected when flow is locally transonic. This is because the gridfins lose effectiveness due to restricted mass flow through the fin from choking resulting in flow spillage and a detached bow shock. The pressure coefficients observed in CFD are

similar to those further upstream closer to the gridfins. This suggests that the degree of flow choking differs between the CFD and WTTs. To better understand the local flow conditions at the grid fins, further processing of the CFD data was required.

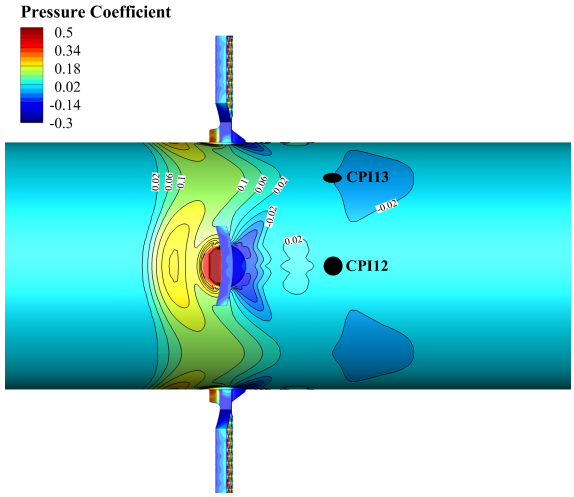


Figure 8: Surface pressure contours at sensor locations 12 and 13 for Mach 2 baseline case

Figure 9 (a) presents close ups of the Mach number field in the vicinity of the gridfins. The first observation made is that the Mach number upstream of the gridfin is not uniform, with a lower Mach number observed closer to the wall and a higher Mach number seen towards the fin tip. Closer to the grid fin, a bow shock decelerates the flow to approximately Mach 0.6 before it enters the cells of the gridfin, is accelerated to Mach 1 and the flow becomes choked. At the exit of the gridfin cells, the flow expands and becomes supersonic. It is also important to note that the Mach contours observed in each of the gridfin cells vary slightly when compared with each other. This is due to local AoA differences caused by the flow direction changing through the bow shock and is illustrated in Figure 9 (b). Upstream of the gridfin holder, a region of recirculating flow is observed, while the high Mach number, triangluar like structure behind the fin is due to flow expansion off the gridfin holder and the tip of the fin. Behind the gridfin holder, a wake region is also observed and is characterised by the low Mach numbers.

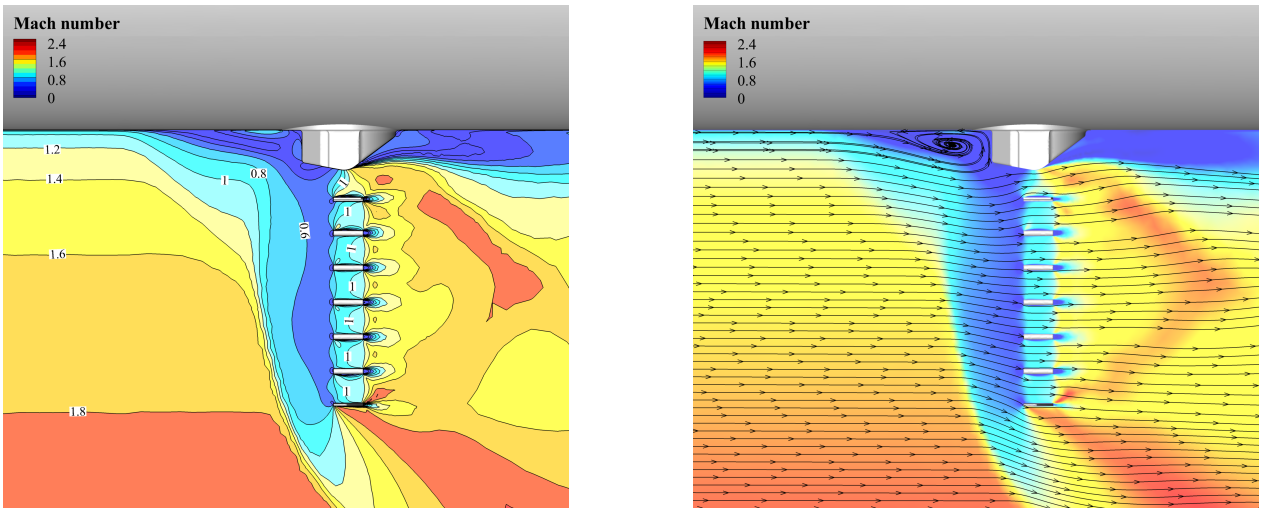


(a) (b)

Figure 9: Gridfin flowfield for Mach 2 baseline case showing (a) Mach contours and (b) flow streamtraces

Finally, a force comparsion between the experimental and numerical datasets is presented in Figure 10. The agreement between datasets is extremely strong, with approximately 2% difference observed. Only results for the axial force are presented as pitching moment and normal forces are approximately equal to zero.

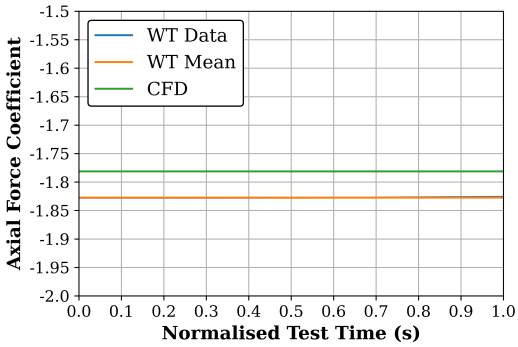


Figure 10: Axial force comparison for Mach 2 baseline case

### 4.2 Baseline Mach 3.6

As was seen in the Mach 2 case, the baseline case at Mach 3.6 also shows very good correlation between CFD and WTT results when comparing the Schlieren photography (see Figure 11).

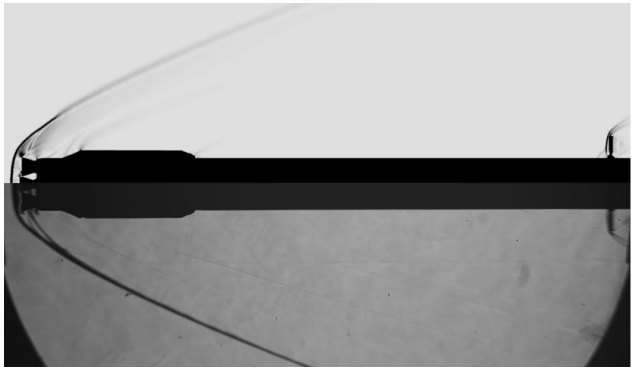

Figure 11: Schlieren photograph comparison for Mach 3.6 baseline case

Figures 12 and 13 present a direct comparison of the pressure coefficient data from WTTs and CFD. Compared with the Mach 2 case, the correlation around the gridfins is significantly improved, but probe 13 results are still in disagreement.

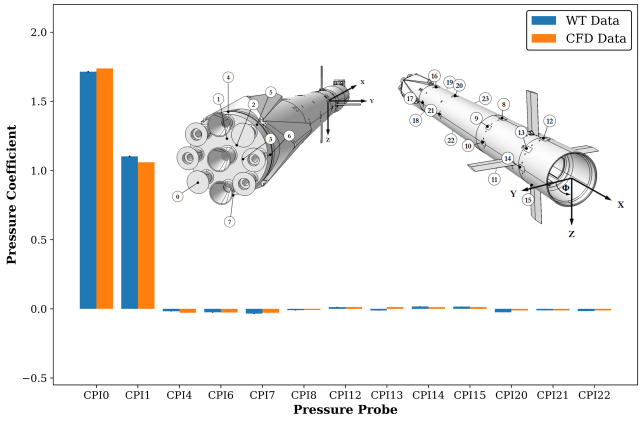


Figure 12: Surface pressure coefficient comparison for Mach 3.6 baseline case for large magnitude pressure coefficients

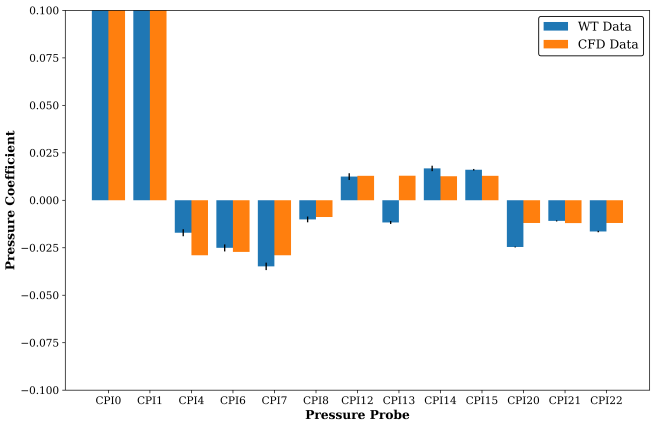


Figure 13: Surface pressure coefficient comparison for Mach 3.6 baseline case for low magnitude pressure coefficients

Observing the surface pressure distribution around sensor 13 in Figure 14, it can be seen that the pressure gradients in this region are quite high. The sensor location is in the middle of a positive pressure region, while a small area of low pressure is located 30mm downstream of the probe, which is more indicative of the WTT measurements. Similar to the Mach 2 case, this suggests that the interactions between the two shocks caused by the fins vary between measured and simulated data. This may may be attributed to the flow behaviour through and around the gridfins.

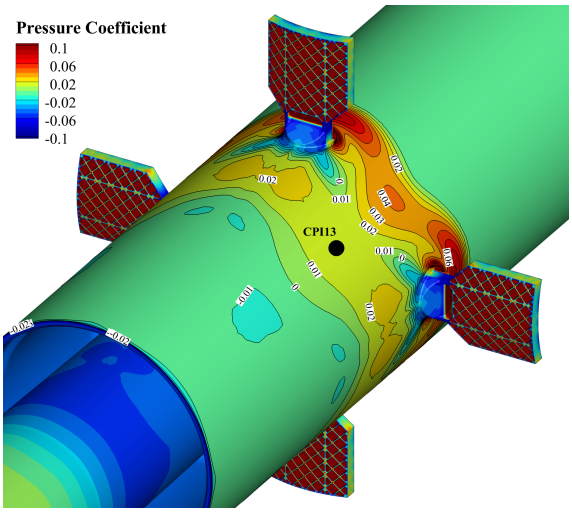


Figure 14: Surface pressure contours at sensor location 13 for Mach 3.6 baseline case

Figure 15 presents the results for the axial force. Correlation is strong, with the CFD data between the upper and lower bounds of the recorded data in the wind tunnel. Overall differences between the average result from the tunnel and the steady state CFD is approximately 2N, which equates to less than 1%.

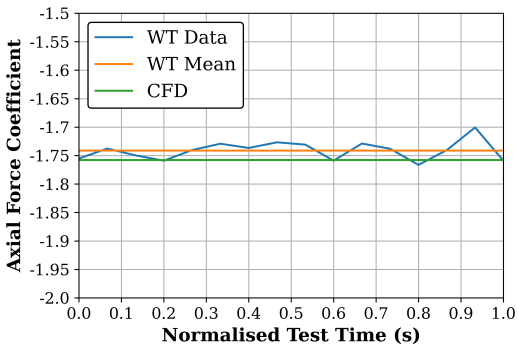


Figure 15: Axial force comparison for Mach 3.6 baseline case

### 4.3 Baseline Mach 5.3

A direct comparison between three Schlieren photographs and the steady state CFD result is presented in Figure 16 below.

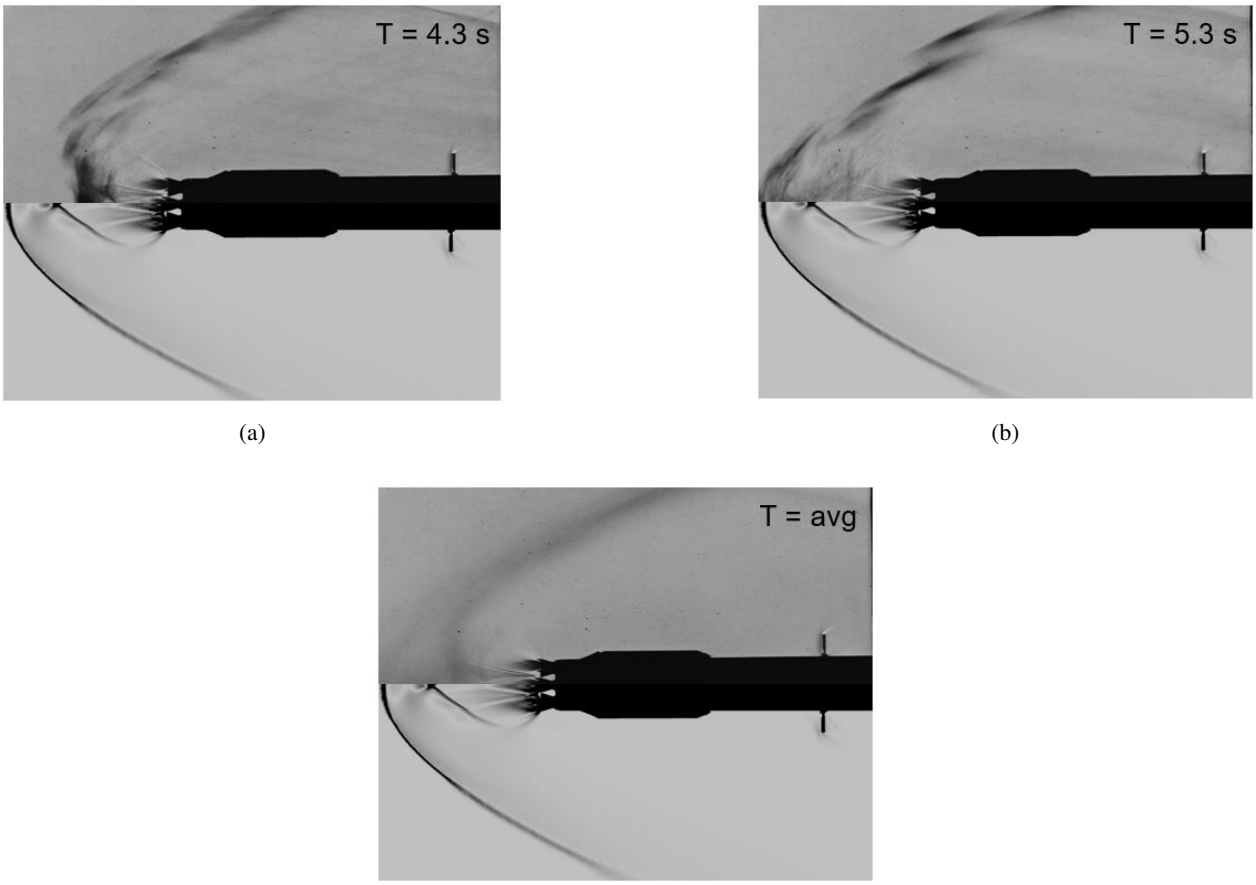


(a) (b)

(c)

Figure 16: Schlieren photograph comparison with CFD for Mach 7 baseline case showing transient nature of the plume flow (a) short plume (b) long plume and (c) averaged plume

The results from the wind tunnel highlight the highly fluctuating flowfield with the three active nozzles. The averaged Schlieren photograph shows two main trends. The first is a high density gradient which is slightly flatter and closer to the nozzle exits, with the second resembling a parabola further away. The latter plume structure best matches the steady state CFD result for this case. Mean pressure coefficient data is presented below in Figure 17. Probes 8 to

15 show relatively good agreement between the wind tunnel results and the CFD data, whereas the mean results from probes 1, 4, 6 and 7 do not show good correlation.

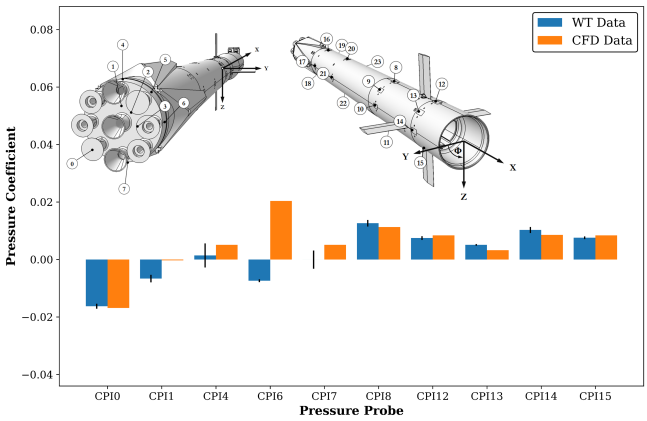


Figure 17: Surface pressure coefficient comparison for Mach 5.3 baseline case

The baseplate pressure coefficient results around pressure sensor 1 are shown below in Figure 18. CFD calculated a pressure coefficient of around -0.001, while WTT data shows approximately -0.006. The pressure coefficient is variable along the baseplate, due to regions of attached and separated flow as seen in Figure 18 (b). While the CFD does not show any areas with a pressure coefficient seen in the WTTs, the large pressure gradients on the baseplate highlight the difficulty in achieving a precise match in this particular location of the model.

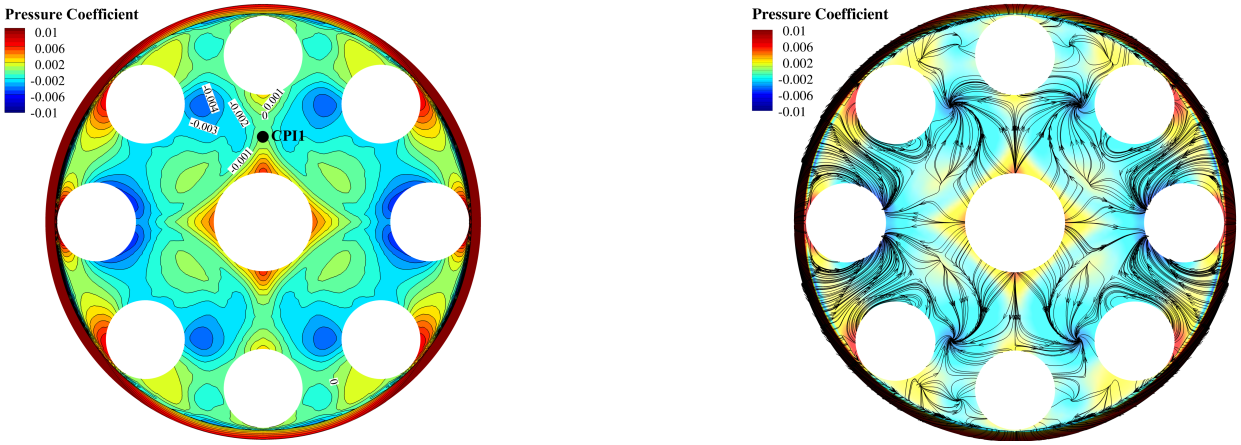


(a) (b)

Figure 18: Mach 5.3 baseline case closeup of baseplate showing (a) banded surface pressure coefficient and (b) overlay of coefficient with surface streamlines of skinfriction

Investigating the correlation variances for probe 4 and 7, it is important to note that the experimental data showed a high standard deviation, with the CFD results closely representing the range of recorded values. Examining a cut plane in Figure 20 at the y = 0 location, it can be seen that the pressure coefficient is fast changing in the region of the sensors. For example, the pressure coefficient recorded just 2 mm closer to the baseplate is half the value of what has been recorded at location 4 and 7. To understand the reasoning behind this, Figure 19 shows two views of the Mach field complete with streamtraces, which highlights the impact of the plume shape on the recirculation zones behind the plume. Figure 19 (a) presents the perspective of the Schlieren images, where the three active jets are seen from the side, while Figure 19 (b) presents a view from the top. Pressure coefficient results for the base region of the model appear to be highly influenced by the shape and overall size of the separated regions due to the presence of the plume.

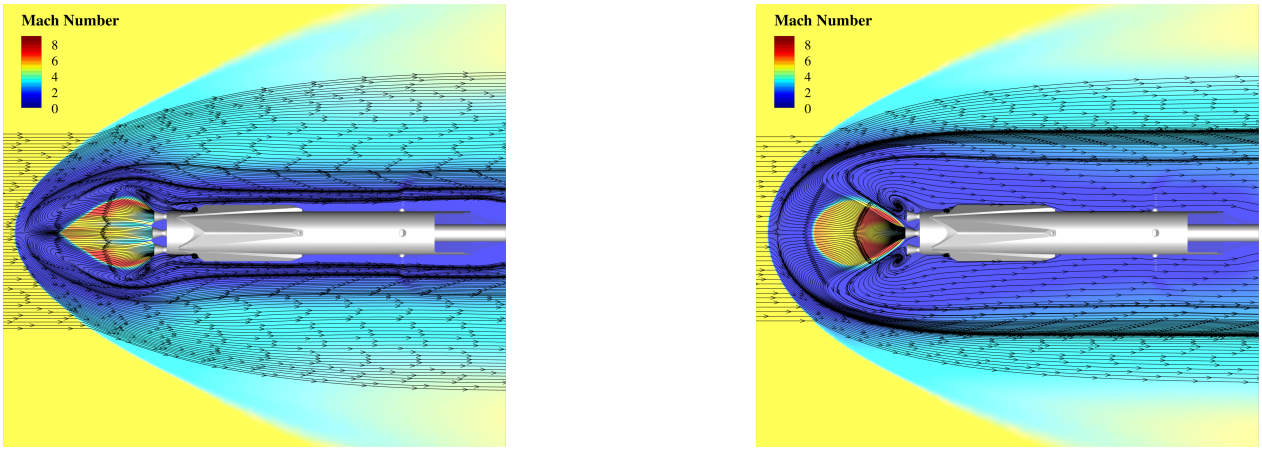


(a) (b)

Figure 19: Mach 5.3 baseline case showing streamtraces and Mach field from (a) top view and (b) side view

The probes located radially around the baseplate are susceptible to large differences in pressure coefficient due to the recirculating flow behind the plume and the location of the separated flow impingment. The lower pressure recorded in the WTTs suggests that the separated region behind the plume is longer than in the numerical reconstruction.

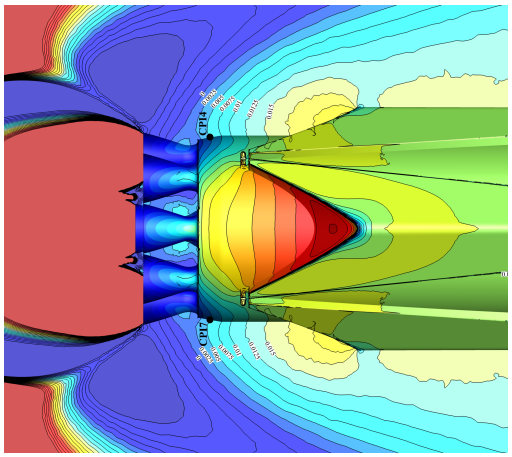


Figure 20: Surface pressure coefficient around sensor 4 and 7 for the Mach 5.3 baseline case

### 4.4 Baseline Mach 7

A direct comparison between three Schlieren photographs and the steady state CFD result is presented in Figure 21 below. The overall plume structure and flow behaviour is identical to the Mach 5.3 case.

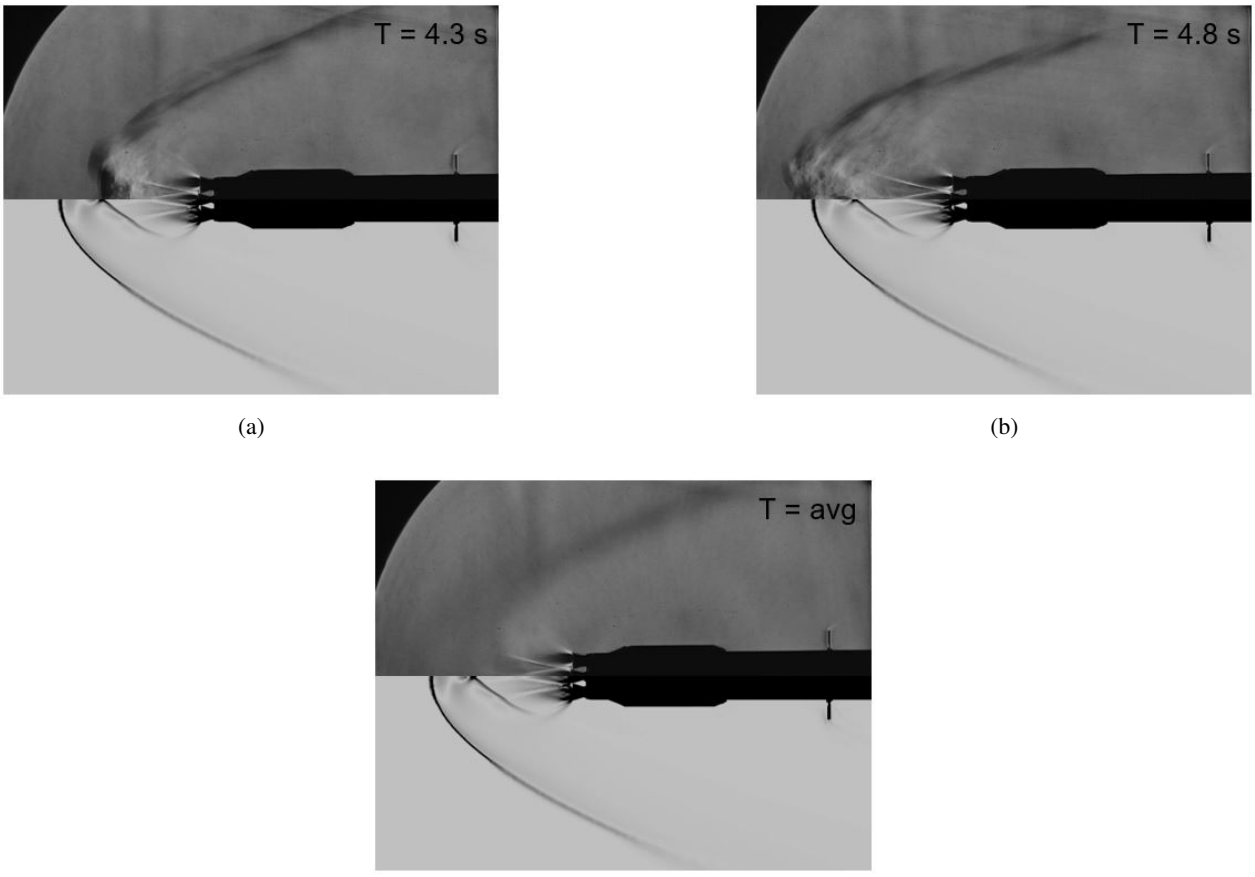


(a) (b)

(c)

Figure 21: Schlieren photograph comparison with CFD for Mach 7 baseline case showing transient nature of the plume flow (a) short plume (b) long plume and (c) averaged plume

An overview of the pressure coefficient distributions in shown in Figure 22. Overall all probes measurements from the wind tunnel show strong correlation with the CFD results. This does not apply to probe 0 or probe 6, which are both located in the base region and gave somewhat different comparisons.

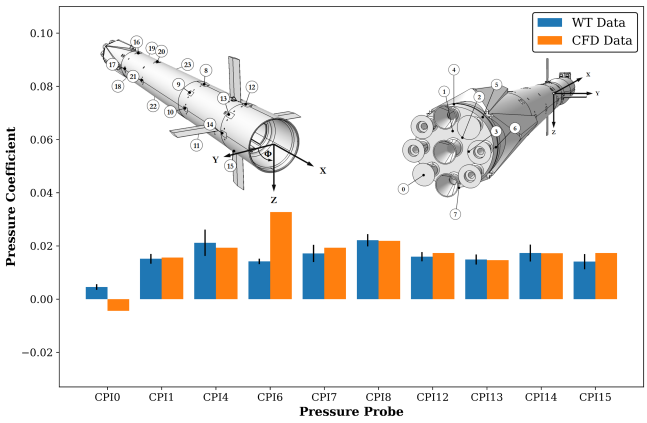


Figure 22: Surface pressure coefficient comparison for Mach 7 baseline case

A closeup of the surface pressure is highlighted in Figure 23. The WT data has a positive pressure coefficient of around 0.005, while CFD shows around -0.005. As can be seen on the contours, large pressure gradients on the surface exist, with approximately one third of the nozzle in the positive range while two thirds are negative. Referring back to Figure 19 (b) from the Mach 5.3 case, the location of flow impingement on the non-acitve nozzles is also dependent on

the size and location of the recirculation zone behind the plume. This is combined with the influence of the expansion of the nozzle flow as it enters the numerical domain. For this case, the disagreement in the surface pressure values is therefore attributed to a small difference in the balance between these two phenomena.

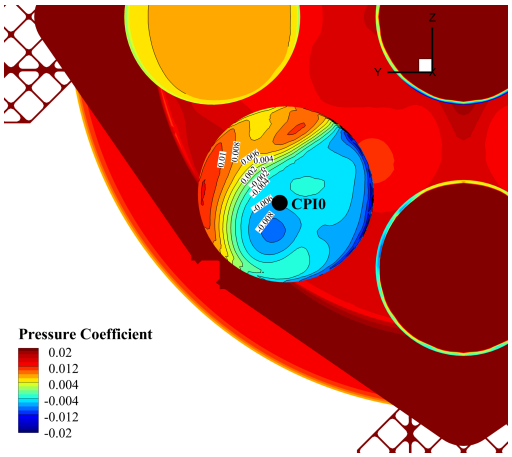


Figure 23: Surface pressure coefficient around sensor 0

Examining a cut plane around the location of pressure sensor 6, it appears to be located at the threshold of a recirculation zone (see Figure 24). This indicates that the separation bubble in the wind tunnel experiments is larger than that predicted by CFD, shifting of the low pressure contours further aft. A possible reason for the discrepency is the difference between the wind tunnel model and the CFD grid. In the baseplate region of the wind tunnel model there is a split where it meets the body of the rocket body. The presence of this feature may have an impact on the pressure distribution in the region of the pressure sensor.

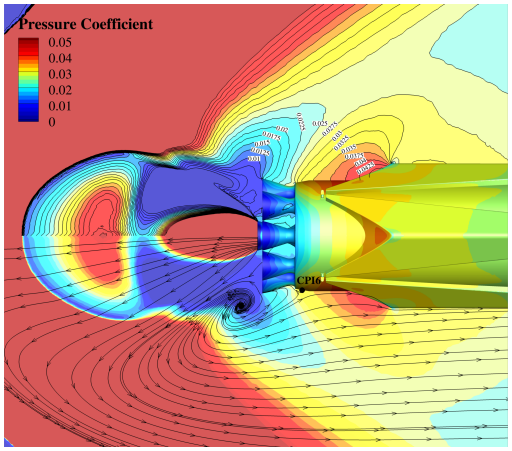


Figure 24: Surface pressure coefficient field around sensor 6

## 5. Conclusion

This paper has presented the results from a CFD reconstruction of wind tunnel experiments for a re-usable first stage launch vehicle as part of the RETPRO project. RETPRO is carried out under a programme of and funded by the European Space Agency - through the Future Launchers Preparatory Programme.

Results from four baseline cases at Mach 7, 5.3, 3.6 and 2 were presented. Cases at Mach 7 and 5.3 were run with three active nozzles, while the two cases at lower Mach numbers represented a free flight condition. The RANS CFD computations were found to perform well at reproducing the forces, pressure measurements and shock structures seen in the unpowered cases. For the tests with active nozzles, the simulations did not perform as well, but trends in the flow topology and plume strucutre were indicative of those seen in the experiments. The main finding was the sensitivity to the pressure coefficient data to the choking of the gridfins, as well as the location and size of recirculation zones. For the cases with active nozzles, this was attributed to the highly unsteady behaviour of the plumes seen in the

wind tunnel. Overall the studies show that RANS simulations using the single equation SA turbulence model perform well compared to experimental data.

## References

[1] Tobias Ecker, Sebastian Karl, Etienne Dumont, Sven Stappert, and Daniel Krause. Numerical study on the thermal loads during a supersonic rocket retropropulsion maneuver. *Journal of Spacecraft and Rockets*, 57(1):131–146, 2020.

[2] D. Kirchheck, A. Marwege, J. Klevanski, J. Riehmer, A. Gülhan, S. Karl, and O. Gloth. Validation of wind tunnel test and cfd techniques for retro-propulsion (retpro): Overview on a project within the future launchers preparatory programme (flpp). In *International Conference on Flight Vehicles, Aerothermodynamics and Re-entry Missions and Engineering (FAR)*, October 2019.

[3] J. Klevanski, T. Ecker, J. Riehmer, E. Dumont B. Reimann, and C. Chavagnac. Aerodynamic studies in preparation for callisto - reusable vtvl launcher first stage demonstrator. In *69th International Astronautical Congress*, October 2018.

[4] M. Laureti and S. Karl. Aerothermal databases and load predictions for retro propulsion-assisted launch vehicles (retalt). *CEAS Space Journal*, January 2022.